**University of Bath**

**Alternative formats**
If you require this document in an alternative format, please contact:
openaccess@bath.ac.uk

# GT2021-59090

## UNSTEADY PRESSURE MEASUREMENTS IN A HEATED ROTATING CAVITY

**Richard W. Jackson, Hui Tang, James A. Scobie, Oliver J. Pountney, Carl M. Sangan, J. Michael Owen and Gary D. Lock**

University of Bath, Bath, United Kingdom

## ABSTRACT

The flow in the heated rotating cavity of an aero-engine compressor is driven by buoyancy forces, which result in pairs of cyclonic and anticyclonic vortices. The resultant cavity flow field is three-dimensional, unsteady and unstable, which makes it challenging to model the flow and heat transfer. In this paper, properties of the vortex structures are determined from novel unsteady pressure measurements collected on the rotating disc surface over a range of engine-representative parameters. These measurements are the first of their kind with practical significance to the engine designer and for validation of computational fluid dynamics. One cyclonic/anticyclonic vortex pair was detected over the experimental range, despite the measurement of harmonic modes in the frequency spectra at low Rossby numbers. It is shown that these modes were caused by unequal size vortices, with the cyclonic vortex the larger of the pair. The structures slipped relative to the discs at a speed typically around 10% to 15% of that of the rotor, but the speed of precession was often unsteady. The coherency, strength and slip of the vortex pair increased with the buoyancy parameter, due to the stronger buoyancy forces, but they were largely independent of the rotational Reynolds number.

## NOMENCLATURE

| | |
|---|---|
| $a$ | inner radius of disc [m] |
| $b$ | outer radius of disc [m] |
| $b'$ | radius of outermost thermocouple on disc diaphragm [m] |
| $d_h$ | hydraulic diameter (= $2(a-r_s)$) [m] |
| $f_d$ | rotational frequency of discs [Hz] |
| $f_s$ | rotational frequency of structures [Hz] |
| $\dot{m}$ | axial throughflow mass flow rate [kg/s] |
| $N$ | disc rotational speed [rpm] |
| $p$ | static pressure [Pa] |
| $\bar{p}$ | mean static pressure [Pa] |
| $\Delta p_f$ | static pressure drop across cavity [Pa] |
| $r$ | radius [m] |
| $r_s$ | outer radius of shaft [m] |
| $t$ | time [s] |
| $T$ | temperature [K] |
| $V$ | rotational velocity of cavity flow [m/s] |
| $W$ | axial throughflow velocity [m/s] |
| $\alpha$ | angular separation of unsteady pressure sensors [rad] |
| $\beta$ | volume expansion coefficient (= $1/T_f$) [K$^{-1}$] |
| $\rho$ | density [kg/m$^3$] |
| $\mu$ | dynamic viscosity [m$^2$/s] |
| $\Delta t$ | time lag between unsteady pressure sensors [s] |
| $\Omega$ | disc angular velocity [rad/s] |
| $\Omega_s$ | angular velocity of rotating structures [rad/s] |

**Dimensionless parameters**

| | |
|---|---|
| $C_p$ | Pressure coefficient (= $(p - \bar{p})/(0.5\rho_f\Omega^2 b^2)$) |
| $\Delta C_{p,f}$ | Cavity pressure drop coefficient (= $\Delta p_f /(0.5\rho_f (W^2 + \Omega^2 a^2))$) |
| Gr | Grashof number (= $\text{Re}_\phi^2 \beta\Delta T$) |
| Ro | Rossby number (= $W/\Omega a$) |
| Re$_z$ | axial Reynolds number (= $\rho_f W d_h/\mu_f$) |
| Re$_\phi$ | rotational Reynolds number (= $\rho_f \Omega b^2/\mu_f$) |
| $\beta\Delta T$ | buoyancy parameter (= $(T_{o,b} - T_f)/T_f$) |
| $\Theta$ | non-dimensional temperature (= $(T_o - T_f)/(T_{o,b} - T_f)$) |

**Subscripts**

| | |
|---|---|
| $b; b'$ | value at $r = b$; value at $r = b'$ |
| $f$ | inlet condition |
| $o$ | value on disc surface |
| $\phi,r,z$ | circumferential, radial and axial direction |
| $1; 2$ | first frequency mode; second frequency mode |

## 1. INTRODUCTION

Figure 1 shows a cross-section of a high-pressure aero-engine compressor. The hot air in the mainstream annulus heats the disc shroud, while cooling air passes through the bore of the discs. When the shroud is hotter than the throughflow, buoyancy-induced flow can occur in the cavity. Figure 2 illustrates a typical flow structure. The circumferential Coriolis forces (which are required for radial flow to occur) are created by the pressure

distribution from counter-rotating vortices in the core, and shear stresses in the Ekman layers. Cold air flows radially outward, before bifurcating into the cyclonic and anticyclonic vortex pair, which have low and high pressures, respectively. Hot air then flows radially inward, where an exchange in enthalpy occurs with the throughflow.
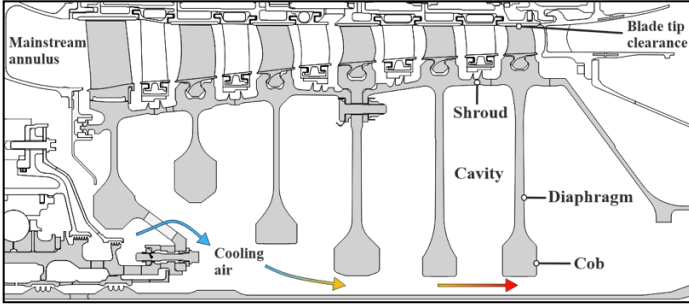


**Figure 1: A cross-section through a modern high pressure aero-engine compressor. Rotating components are shaded grey. Adapted from [1].**
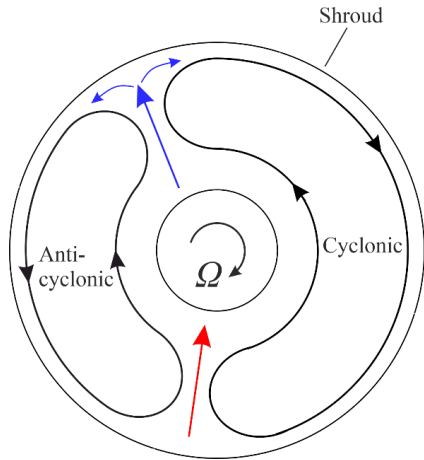


**Figure 2: The flow structures in a heated rotating cavity (*r-ϕ* plane). Adapted from [2].**

## 1.1 Governing parameters

A detailed review into buoyancy-induced flow in rotating cavities is provided by Owen and Long [3]; only a brief overview of the relevant literature is provided here. Buoyancy-induced flow is principally governed by the Grashof number, which combines the effects of rotation and the buoyancy parameter, *βΔT*:

$$\text{Gr} = \text{Re}_\phi^2 \beta \Delta T \tag{1}$$

The influence of the throughflow is described by the Rossby number:

$$\text{Ro} = \frac{W}{\Omega a} \propto \frac{\text{Re}_z}{\text{Re}_\phi} \tag{2}$$

$\text{Re}_z$, $\text{Re}_\phi$ and other variables are defined in the nomenclature. For conditions where Ro is low and *βΔT* is high, flow in the cavity is driven by the buoyancy-induced flow, and the throughflow does not penetrate far into the cavity. If Ro is sufficiently high, a toroidal vortex forms in the inner (low radius) region, as the throughflow impinges on the downstream disc and recirculates. The existence of the toroidal vortex in a heated cavity has been demonstrated using velocity measurements [4, 5], heat transfer measurements [6 - 8] and computations [9].

## 1.2 Cavity flow field

The existence of a cyclonic/anticyclonic vortex pair in the cavity flow field was first shown experimentally in a heated cavity rig (with *a/b* = 0.1 and without a central shaft) using smoke visualization [2]. The number of vortex pairs was found to increase to two or three as the axial width of the cavity inlet was reduced. These findings were validated in a cavity with a central shaft by Bohn *et al.* [10], who used flow visualization images to show that the vortices can be of unequal size. Laser Doppler Anemometry (LDA) velocity measurements were collected by Owen and Powell [11] in a cavity in which only one disc was heated (as the other housed an optical window for the laser). Using spectral analysis techniques on the velocity data, they estimated that up to three vortex pairs existed in the cavity flow field. Long *et al.* [4] used similar analytical techniques on their velocity measurements, from which they identified two vortex pairs in the rotating flow.

LDA measurements in the mid-axial plane of the cavity by Farthing *et al.* [2] revealed that the average velocity of the core between the Ekman layers in the buoyancy-driven region, can rotate at a speed lower than that of the discs. The difference in the rotational speed, or the *slip*, was as high as 10% of the disc speed (*i.e.* $V_\phi/\Omega r = 0.9$). They found that Ro can also affect the slip of the core, which they believed was caused by breakdown of the toroidal vortex. The main modes of vortex breakdown in an *isothermal* cavity without a central shaft are described in detail by Owen and Pincombe [12]. Velocity measurements by Long *et al.* [4] show that an increase in Ro causes an increase in $V_\phi/\Omega r$ at low radius, but a reduction at high radius. Computations by Pitz *et al.* [7], reveal that an increase in Ro results in more air from the throughflow penetrating the cavity, which causes an increase in radial velocity fluctuations. Experimental evidence shows that an increase in *βΔT* also causes an increase in slip [2, 4, 11]. Long *et al.* [4] suggest that this is due to stronger buoyancy forces that destabilize the throughflow, causing an increase in radial mixing.

Recent numerical simulations reveal further detail about the cavity flow field. Instantaneous flow field 'snapshots' from the computations of Puttock-Brown and Rose [13] show that the vortex pairs can be of unequal size and strength, with a much smaller second cyclonic vortex in-between two larger anticyclonic vortices. They calculated the slip of the core to be around 6% using the measurements from unsteady pressure sensors on the stationary shaft. Simulations produced by Fazeli *et al.* [5] demonstrate the instability of the flow field, showing a vortex structure which changes between one and two pairs over

time; they validated the number of structures using spectral analysis techniques on LDA velocity measurements.

This paper presents an analysis of unsteady pressure measurements, collected on the rotating disc surface in the central cavity of the Bath Compressor-Cavity Rig over a range of the important non-dimensional parameters. This measurement technique has been successfully used in rotor-stator systems to identify large-scale rotating flow structures [14, 15], and more recently, on the disc surface of a *closed* rotating cavity of the Bath rig [16]. This is the first time that unsteady pressures have been directly measured on the rotating surface of a heated rotating cavity, which is open to the cooling throughflow at the inner radius. The findings from the experiments presented in this paper will be of direct value to computational researchers seeking validation of their simulations.

Section 2 describes the Bath Compressor-Cavity Rig and the high frequency pressure sensors. The results summarizing the effect of the non-dimensional parameters are explained in Section 3 and the conclusions are summarized in Section 4.

## 2. BATH COMPRESSOR-CAVITY RIG

Measurements were collected from the Bath Compressor-Cavity Rig, which was designed and constructed in partnership with Torquemeters Ltd. The rig is illustrated in Fig. 3 and a detailed description of the design and operational limits of the facility are given by Luberti *et al.* [17].

The rig features an overhung disc drum mounted at one end of a shaft assembly, driven by a 30 kW motor via a belt at the opposite end to the discs. The disc drum can operate at speeds in the range $N = 800 - 8,000$ rpm, equivalent to $Re_\phi \sim 3x10^5 - 3x10^6$; the speed is measured by the motor encoder to within $\pm$ 10 rpm. Quiescent, ambient air at room temperature is drawn through the annulus between a stationary shaft and the bore of the rotating drum. The air passes around the bearing sleeve of the drive-shaft unit, and through to an extraction unit (not shown), which can create throughflow mass-flow rates of up to 0.15 kg/s. The flow rate is measured by a thermal mass flow meter to within $\pm$ $5x10^{-4}$ kg/s. The rig can achieve a maximum $Re_z \sim 4x10^4$ and Ro $\sim 2$.

The disc drum comprises four titanium discs, creating three rotating cavities. The surfaces of the upstream and downstream cavities were insulated with low conductivity Rohacell foam. Heat and mass transfer between the throughflow and upstream/downstream cavities were prevented by modular Rohacell inserts. For the experiments presented in this paper, the central cavity was open to the throughflow. The width of the cavity at the inner radius can be reduced (and even *closed*), by the attachment of aluminium rings. The shroud temperature of the central cavity was controlled by six circular-heater 2 kW elements, which could achieve shroud temperatures in excess of 100°C, equivalent to $\beta\Delta T \sim 0.28$.
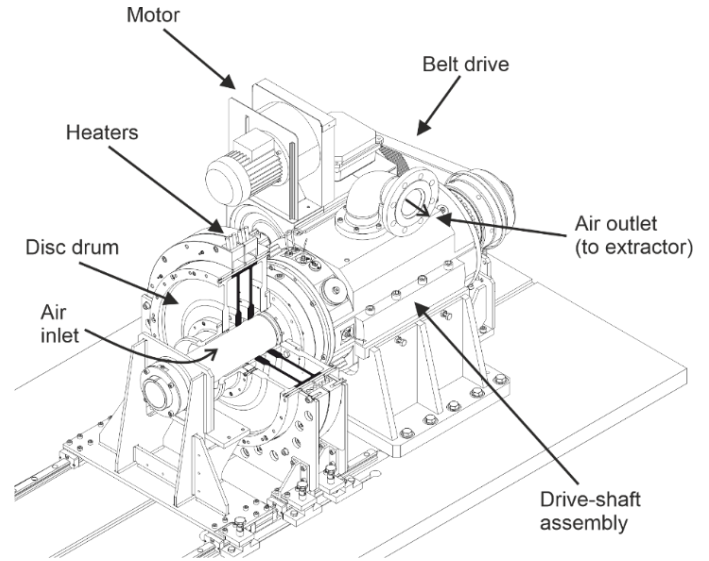


**Figure 3: The experimental rig showing a section view of the disc drum. The cavity test section is shaded black.**

Figure 4 shows a cross-section of the central cavity and the relevant instrumentation. The diaphragm and cob of the upstream and downstream discs contain K-Type thermocouples, which were embedded directly in circumferential grooves in the disc surface to minimize thermal disturbance errors – see Luberti *et al.* [17]. In addition, thin foil thermocouples were mounted under the disc shroud to measure the local temperature, which is required to find the buoyancy parameter, $\beta\Delta T$. For these experiments, the disc temperature measurements were principally used to determine when a steady-state condition had been reached, and further detail on how this is defined is described below. Two fast-response pressure sensors (Kulite XCQ-080 series) were mounted in the downstream disc, flush with the surface, at a radius ratio of $r/b = 0.85$, and with a circumferential separation of $\alpha = 35°$. The sensors were mounted at a high radius, in order to be confident that the measurements would be in the buoyancy-induced flow region where the cyclonic/anticyclonic vortices occur.

The wires from the rotating instrumentation were routed to the back surface of the disc drum and passed through the drive unit to a Datatel telemetry system. The thermocouples were pinned into low-frequency transmitter modules, which each contain a PT100 Resistance Temperature Detector (RTD) to measure the cold-junction temperature. The wires from the unsteady pressure sensors were connected to a separate high-frequency module. The data from the telemetry were transmitted to a receiver via an antenna. The thermocouple data were compensated using the cold-junction temperature from the RTD and converted to a temperature using a known calibration. The estimated combined uncertainty of the rotating thermocouples can be described by a standard deviation of around $\pm$ 0.5 °C.
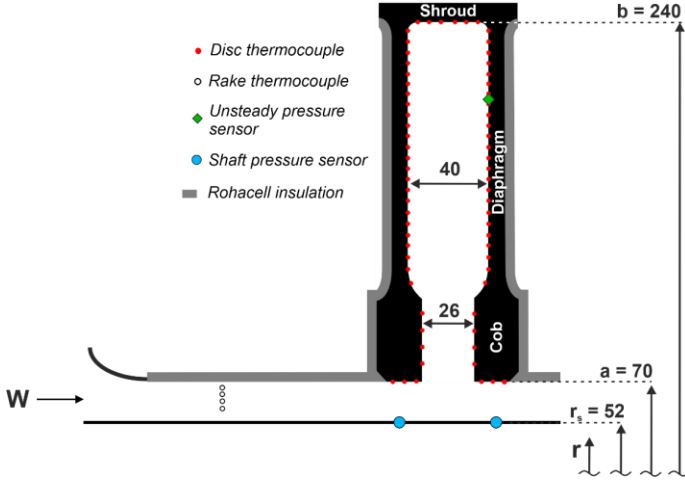
**Figure 4: Cross-section of the instrumented test-section, showing disc and rake thermocouple locations and the unsteady pressure sensors on the disc. The main dimensions are given in millimeters.**

The data from the pressure sensors passed through a 1 kHz low-pass filter before being sampled at 10 kHz to minimize effects of signal aliasing. For each test, a 100 second sample was collected (equivalent to $10^6$ data points per test). At 8,000 rpm the equivalent disc frequency is $f_d = 133$ Hz. The measured rotational frequency of the structures will be lower, as the sensors are collecting data in the *rotating frame* of reference. Therefore, the frequency of the low-pass filter is sufficiently high to satisfy the Nyquist criterion. The unsteady pressure data were acquired by a National Instruments NI 9215 data logger. The uncertainty in the absolute pressure measurement, described by the standard deviation, is around ± 1.5 mbar.

To identify if vortex breakdown occurred at certain conditions, the pressure drop across the cavity was measured on the surface of the stationary shaft by two static pressure sensors (ESI PR3204 series). These sensors were individually calibrated in-house using a Druck pressure calibrator, which supplied known, pre-set pressure values to the sensors.

Data from the thermocouples and shaft pressure sensors were acquired at a sampling rate of 10 Hz. The normalized temperature, $\Theta$, was used to assess whether steady-state conditions had been reached in the cavity.

$$\Theta = \frac{T_o - T_f}{T_{o,b'} - T_f} \qquad (3)$$

Here, $T_f$ is the average temperature of the throughflow upstream of the cavity and $T_{o,b'}$ is the temperature measured from the thermocouple at the highest radius on the diaphragm (*i.e.* closest to the shroud). A steady-state condition was defined to be when the median average of $\Theta$ for each disc thermocouple changed by less than 0.01 between a pair of ten-minute intervals.

The ranges for the experimental parameters are summarized in Table 1. A total of 19 experiments were performed.

| | Parameter | $N$ [rpm] | $\Delta T$ [°C] | $\dot{m}$ [kg/s] |
|---|---|---|---|---|
| a) | Range | 800 – 8,000 | 30 - 80 | 0.024 – 0.099 |

| | Parameter | $\beta\Delta T$ | $Re_\phi$ | Gr | $Re_z$ | Ro |
|---|---|---|---|---|---|---|
| b) | Range | 0.11 - 0.28 | $3.2x10^5$ – $3.1x10^6$ | $1.4x10^{10}$ – $2.4x10^{12}$ | $6.9x10^3$ – $2.9x10^4$ | 0.1 – 1.0 |

**Table 1: a) Dimensional and b) non-dimensional experimental parameter ranges.**

## 3.  ANALYSIS OF PRESSURE MEASUREMENTS

The spectral analysis method is first described, before being applied to an example case to demonstrate how the slip of the structures and the number of vortex pairs is quantified. The effects of the main non-dimensional parameters ($\beta\Delta T$, $Re_\phi$ and Ro) on the circumferential pressure distribution are then discussed.

### 3.1  Analytical method for an example case

The location of both unsteady pressure sensors in the $r$-$\phi$ plane of the cavity is shown in Fig. 5, alongside a schematic of a single vortex pair structure. The sensors are separated by a circumferential angle of $\alpha = 35°$. The structures rotate about the disc axis at an angular velocity, $\Omega_s$:
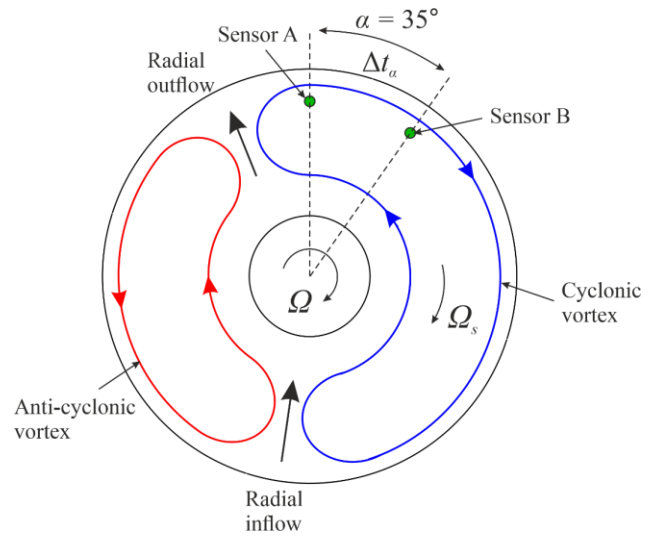
$$\Omega_s = \frac{\alpha}{\Delta t_\alpha} \qquad (4)$$



**Figure 5: Location of unsteady pressure sensors (note: $r/b = 0.85$).**

The time lag between both sensors, $\Delta t_\alpha$, can be found through the cross-correlation of both signals. It follows that the rotational frequency of the structures, $f_s$, is:

$$f_s = \frac{\alpha}{2\pi\Delta t_\alpha} \qquad (5)$$

The pressure coefficient, $C_p$, is defined from the difference between the static pressure, $p$, and the mean of the data sample, $\bar{p}$:

$$C_p = \frac{p - \bar{p}}{0.5\rho_f\Omega^2 b^2} \qquad (6)$$

The frequency spectra from the Fourier transform of the pressure measurements are shown in Fig. 6 for an example case where $Re_\phi = 8\times10^5$, $\beta\Delta T = 0.28$, $Gr = 1.9\times10^{11}$ and $Ro = 0.2$. The frequency is normalized with respect to the rotational frequency of the discs ($f_d$). As the sensors are fixed on the rotating disc surface, the frequency spectra show the *relative* movement of any structures. Both sensors detect a dominant frequency at around 13% of the disc speed, and a smaller secondary peak at twice this frequency. They also show similar magnitudes of $C_p$ and little noise and significant frequency content other than the two modes.



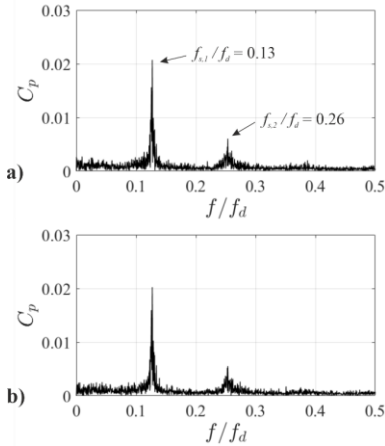**Figure 6: Frequency spectra of the pressure measurements from a) Sensor A and b) Sensor B ($Re_\phi = 8\times10^5$, $\beta\Delta T = 0.28$, $Gr = 1.9\times10^{11}$, $Ro = 0.2$).**

It is reasonable to assume that the dominant peak, $f_{s,1}$, corresponds to the rotational frequency of the vortex structures. This assumption is required to produce Fig. 7, which shows how the circumferential pressure distribution varies with time, over 400 structure revolutions. The pressure distribution is in the frame of reference of the rotating structures ($2\pi f_{s,1}t$). The red and blue colors indicate positive and negative pressures, respectively, which can be attributed to the anticyclonic and cyclonic vortices.

Only one vortex pair is visible from either contour plot. This may seem counter-intuitive given the two frequency peaks in Fig. 6, but an explanation for the second mode is given below. It may be possible that a second, smaller vortex pair does exist, but at a radius lower than that of the sensor location. Smaller, secondary cyclonic vortices are shown in the results of some numerical simulations [5, 13]. Figure 7 also shows that the vortices can deviate from the dominant rotational frequency, highlighting their unsteadiness. Therefore, an ensemble average across the full data sample will result in an underprediction of

the true pressure magnitude in the cavity. This wandering effect partly explains why the magnitudes of $C_p$ in the frequency spectra of Fig. 6 are much lower than the amplitudes in the contour plots.
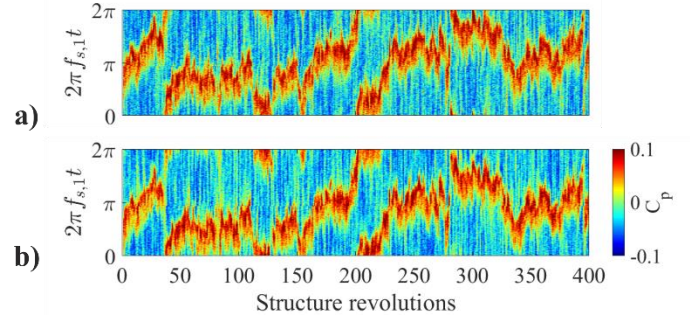


**Figure 7: Circumferential pressure distribution over time, measured by a) Sensor A and b) Sensor B.**

Figure 8 shows an ensemble average of the circumferential pressure distribution between the 50th and 100th structure revolution, where the rotational frequency of the structures is stable. This clearly shows one vortex pair. The phase lag between the pressure measurements of both sensors is around 35°, equal to the sensor separation angle, $\alpha$, and confirming that the dominant mode does correspond to the rotational frequency of the structures. The vortices are unequal in size: the anticyclonic vortex ($C_p > 0$) covers a smaller angle, but with a greater pressure magnitude than that of the cyclonic vortex ($C_p < 0$). This finding is consistent with those of other experimental and computational researchers [5, 10, 13]. The second frequency mode in Fig. 6 can be attributed to the uneven sizes of the two vortices, *i.e.* the greater the magnitude of the second mode, the more uneven the vortex pair. Further evidence of this is provided in the Appendix and the discussion on the effect of Ro in Section 3.2. The uncertainty in the value of $C_p$ in Fig. 8 is approximately $\pm 0.003$ (one standard deviation). This is based on the uncertainties in the relative pressure measurement, ($p - \bar{p}$), and the reference pressure ($0.5\rho_f\Omega^2 b^2$). The uncertainty in ($p - \bar{p}$) is less than $p$, as the subtraction of the mean quantity removes any bias errors.
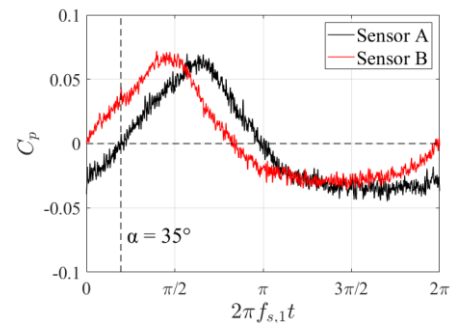


**Figure 8: Ensemble averages of $C_p$, between the 50th and 100th structure revolution.**

## 3.2 Influence of non-dimensional parameters

For conciseness, the data presented in this sub-section is solely from Sensor A. Figure 9 shows the effect of $\beta\Delta T$ on the slip of the structures and the circumferential pressure variation over 200 structure revolutions. At $\beta\Delta T = 0.1$, a small peak exists in the frequency spectrum around $f_{s,1}/f_d = 0.07$, but no periodic structures are detected in the corresponding contour plot (Fig. 9a). This is because either they are too weak to detect, owing to low buoyancy forces, or because the vortex pair is restricted radially outward from the pressure sensors. Figure 9b shows that at $\beta\Delta T = 0.19$, the two structures are now discernible, but highly unsteady. A second mode may be developing, indicative of the unequal size of the vortex pair. Increasing $\beta\Delta T$ further results in an increase in the magnitude and frequency of the dominant mode, and a corresponding improvement in the coherency of the structures (Fig. 9c). The formation and strengthening of the vortex pair with $\beta\Delta T$ results in an increase in slip, as reported by other experimenters [2, 4, 11]. As the radial flow strengthens with $\beta\Delta T$, it may be drawing in more low momentum fluid from the throughflow, thereby increasing the slip.
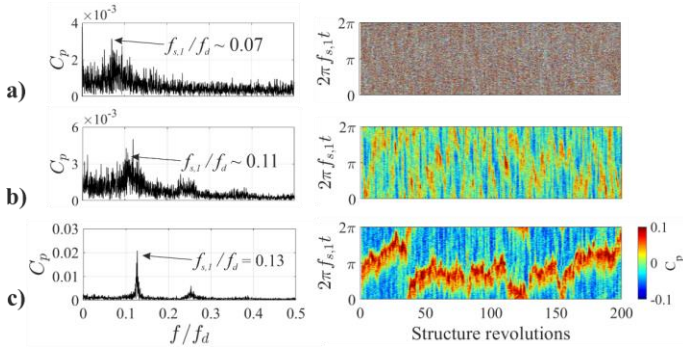


**Figure 9: Effect of $\beta\Delta T$ on the frequency spectrum and circumferential pressure variation for a) $\beta\Delta T = 0.12$, b) $\beta\Delta T = 0.19$ and c) $\beta\Delta T = 0.28$. $Re_\phi = 8x10^5$; Ro = 0.2.**

The slip of the structures is broadly independent of $Re_\phi$, as shown by the cases presented in Fig. 10; here the slip is between 12% and 13% of the disc speed for $\beta\Delta T > 0.24$. The ensemble plots on the right are averaged over ten structure revolutions where the rotational frequency of the structures is stable. The windowing region is indicated by the white dashed lines in the corresponding contour plots. The ensemble averages for the cases here only show one vortex pair, which is of unequal size, with a smaller anticyclonic vortex. The different-sized vortices are identified in the frequency spectra by smaller, second harmonic modes. The ensemble averages show that the circumferential distributions of $C_p$ are similar across the rotational speeds presented. The raw pressure amplitude of the ensemble average for the highest $Re_\phi$ case in Fig. 10d ($\sim$ 1 kPa) is an order of magnitude higher than the lowest $Re_\phi$ case in Fig. 10a ($\sim$ 100 Pa). The apparent elevated level of noise in the ensemble average of Fig. 10a is due to the smaller pressure amplitudes. At $Re_\phi = 3.1x10^6$ (Fig. 10d), the contour plot suggests significant unsteadiness, which has caused the pressure

content in the frequency spectrum to be more evenly distributed. It is not currently understood what may be causing the sudden increase in unsteadiness at higher values of $Re_\phi$.
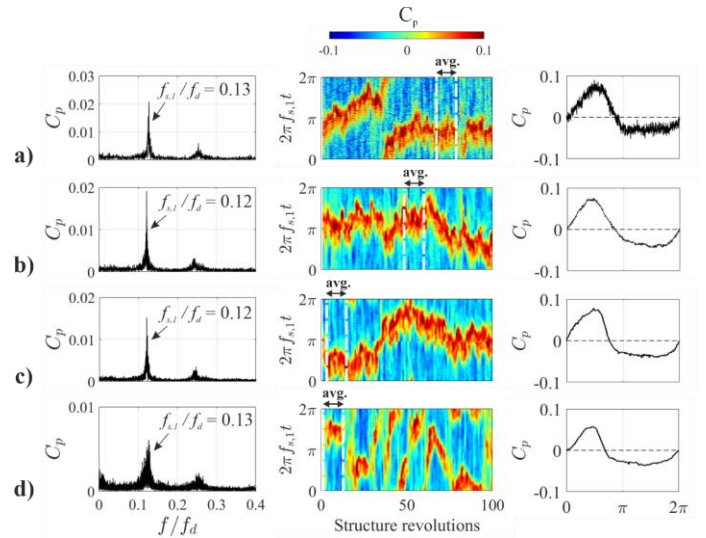


**Figure 10: Effect of $Re_\phi$ on the frequency spectrum, circumferential pressure distribution and ensemble averages of pressure for a) $Re_\phi = 0.8x10^6$, b) $Re_\phi = 1.6x10^6$, c) $Re_\phi = 2.4x10^6$ and d) $Re_\phi = 3.1x10^6$. $\beta\Delta T = [0.24, 0.28]$; Ro = 0.2.**

Figure 11 presents the effect of Ro on the slip and pressure distribution of the vortices. Increasing from Ro = 0.2 to Ro = 0.4 results in an increase in the slip of the structures; there is also a corresponding increase in the pressure magnitude, which is reflected in both the frequency spectra and ensemble averages. Again, only one vortex pair is detected. The vortex pair is closer in size at Ro = 0.4, which is shown by the ensemble average describing a near-symmetric sinusoid and by the smaller second harmonic in the frequency spectrum. An initial increase in slip with Ro can be explained by more throughflow entering the cavity and reducing the overall momentum of the cavity flow. This behaviour has been shown to occur in the numerical simulations of a heated rotating cavity with an axial throughflow [7]. The corresponding increase of $C_p$ magnitude with Ro may therefore be caused by a subsequent strengthening of the radial flow and vortex pair.

A further increase to Ro = 0.8, causes a *reduction* in the slip of the structures. Here, the ensemble average reveals that the size of the two vortices are almost identical, and consequently there is not a second harmonic peak in the frequency spectrum. Previous heat transfer measurements collected from the Bath Compressor Cavity Rig suggest that a toroidal vortex exists in the inner region of the cavity at Ro = 0.8 [8]; this will cause the angular momentum in the inner region to increase, limiting low momentum throughflow from reaching the outer region where the buoyancy-induced vortices occur. The contour plots suggest that the unsteadiness in the vortices may have increased slightly at Ro = 0.8. This could be a consequence of velocity fluctuations

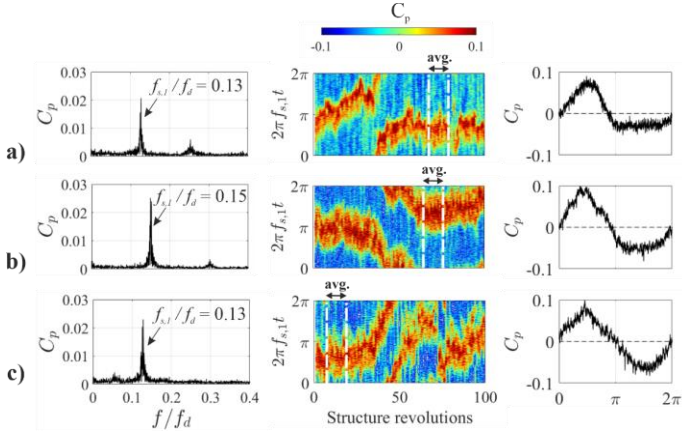in the core, which numerical simulations have shown to increase with Ro [7].



**Figure 11: Effect of Ro on the frequency spectrum, circumferential pressure distribution and ensemble averages of pressure for a) Ro = 0.2, b) Ro = 0.4 and c) Ro = 0.8. $\beta\Delta T$ = [0.26, 0.28]; $Re_\phi$ = 8x10$^5$.**

The variation of Ro with slip is presented in Fig. 12a, for all conditions tested where $\beta\Delta T > 0.24$. The trend follows the same behavior as that shown in Fig. 11. It is possible that the peak slip of the structures at Ro = 0.4 is a consequence of breakdown of the toroidal vortex. Vortex breakdown can be inferred from the measured static pressure drop across the cavity, $\Delta p_f$. The unsteadiness and mixing losses associated with vortex breakdown can cause a significant increase in pressure drop, as found by Owen and Pincombe [12]. The static pressure drop is converted to a pressure coefficient, using a dynamic pressure which combines the velocity contribution of the throughflow and rotational speed at the inner radius, $a$:

$$\Delta C_{p,f} = \frac{\Delta p_f}{0.5\rho(W^2 + \Omega^2 a^2)} \qquad (7)$$

Figure 12b shows the effect of Ro on the pressure drop. Although neither $Re_z$ and $Re_\phi$ are fixed, experimental evidence collected from this rig suggests that the flow structure in the annulus and inner region is predominantly a function of Ro [8]. The discontinuity in pressure around Ro = 0.5 is indicative of vortex breakdown, and it exhibits a similar behavior to that shown by Owen and Pincombe [12]. The maxima of pressure-drop and slip occur at similar Rossby numbers, suggesting that vortex breakdown is influencing the slip. Breakdown of the toroidal vortex would encourage significant mixing between the throughflow and cavity flow.

Only one vortex pair was detected in the 19 experimental cases. Experiments in a *closed* rotating cavity of the Bath rig measured between three and four pairs, with the flow structures experiencing almost solid body rotation ($\Omega_s/\Omega > 0.99$) [16]. This suggests that, along with the slip, the interaction of the

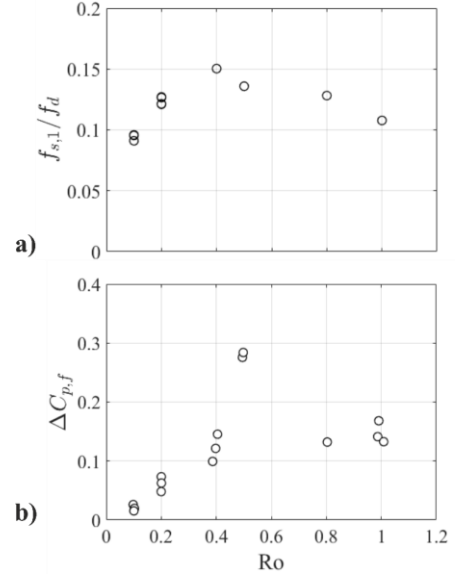throughflow with the cavity flow has a strong influence on the number of vortex pairs.



**Figure 12: a) Slip of structures and b) pressure drop across the cavity as a function of Ro (for cases where $\beta\Delta T > 0.24$).**

## 4. CONCLUSIONS

Unsteady pressure measurements have been collected from the Bath Compressor-Cavity Rig over a range of the relevant non-dimensional parameters: $3.2x10^5 < Re_\phi < 3.1x10^6$; $0.11 < \beta\Delta T < 0.28$; $1.4x10^{10} < Gr < 2.4x10^{12}$; $0.1 < Ro < 1.0$. These measurements are the first of their kind with practical significance to the engine designer and for validation of computational fluid dynamics.

The measurements revealed that one cyclonic/anticyclonic vortex pair was detected across the range of conditions tested. Although the frequency spectra showed two peaks at certain conditions (Ro < 0.4), it has been demonstrated that the magnitude of the second peak describes the relative size of the vortices. For conditions where Ro < 0.4, the cyclonic vortex is the larger of the pair.

The fundamental peak was shown to correspond to the movement, or slip, of the vortex pair relative to the rotating discs. For conditions where coherent, periodic structures were detected (*i.e.* $\beta\Delta T > 0.24$), the slip varied between 10% and 15% of the disc speed. Although the slip was characterized by a dominant peak in the frequency spectra, the vortex pairs were susceptible to unsteadiness and often wandered faster and slower than the typical slip frequency.

The coherency, strength and slip of the vortex pair increased with $\beta\Delta T$ due to the stronger buoyancy forces, while these properties were largely unaffected by $Re_\phi$. The slip and relative size of the vortices were shown to be dependent on Ro, with the slip reaching a maximum of 15% at Ro = 0.4. This coincided with the value of Ro at which vortex breakdown occurs, which was indicated by static pressure measurements made across the

cavity in the throughflow. The enhanced mixing between the low momentum throughflow and the cavity air caused by vortex breakdown is expected to be responsible for the peak in slip.

## REFERENCES

[1] Fitzpatrick, J. N., 2013, "Coupled Thermal-Fluid Analysis with Flowpath-Cavity Interaction in a Gas Turbine Engine," Purdue University. Master's Thesis.

[2] Farthing, P. R., Long, C. A., Owen, J. M., and Pincombe, J. R., 1992, "Rotating Cavity with Axial Throughflow of Cooling Air: Flow Structure," *ASME. J. Turbomach.*, **114**(1), pp. 237-246.

[3] Owen, J. M., and Long, C. A., 2015, "Review of Buoyancy-Induced Flow in Rotating Cavities," *ASME. J. Turbomach.*, **137**(11), pp. 1-13.

[4] Long, C. A., Miche, N. D. D., and Childs, P. R. N., 2007, "Flow Measurements Inside a Heated Multiple Rotating Cavity with Axial Throughflow," *Int. J. Heat Fluid Flow*, **28**(6), pp. 1391-1404.

[5] Fazeli, S. M., Kanjirakkad, V., and Long, C. A., 2020, "Experimental and Computational Investigation of Flow Structure in Buoyancy Dominated Rotating Cavities," ASME Paper No. GT2020-14683.

[6] Günther, A., Uffrecht, W., Odenbach, S., 2012, "Local Measurements of Disc Heat Transfer in Heated Rotating Cavities for Several Flow Regimes," *ASME. J. Turbomach.*, **134**(5), p. 051016.

[7] Pitz, D. B., Chew, J. W. and Marxen, O., 2019, "Effect of an Axial Throughflow on Buoyancy-Induced Flow in a Rotating Cavity," *Int. J. Heat Fluid Flow*, Vol. 80, 108468.

[8] Jackson, R., Luberti, D., Tang, H., Pountney, O., Scobie, J., Sangan, C., Owen, J. M., and Lock, G. D., 2020, "Measurement and Analysis of Buoyancy-Induced Heat Transfer in Aero-Engine Compressor Rotors," ASME *J. Eng. Gas Turbines Power*

[9] Gao, F., and Chew, J. W., 2020, "Ekman Layer Scrubbing and Shroud Heat Transfer in Centrifugal Buoyancy-Driven Convection," ASME Paper No. GT2020-16220.

[10] Bohn, D. E., Deutsch, G. N., Simon, B., and Burkhardt, C., 2000, "Flow Visualisation in a Cavity with Axial Throughflow," ASME Paper No. 2000-GT-280.

[11] Owen, J. M., and Powell, J., 2006, "Buoyancy-Induced Flow in a Heated Rotating Cavity," ASME *J. Eng. Gas Turbines Power*, **128**(1), pp. 128 – 134.

[12] Owen, J. M., and Pincombe, J. R., 1979, "Vortex Breakdown in a Rotating Cylindrical Cavity," *J. Fluid Mech.*, **90**(1), pp. 109-127.

[13] Puttock-Brown, M. R., and Rose, M. G., 2018, "Formation and Evolution of Rayleigh-Bénard Streaks in Rotating Cavities," ASME Paper No. GT2018-75497.

[14] Beard, P. F., Gao, F., Chana, K. S., and Chew, J. W., 2017, "Unsteady Flow Phenomena in Turbine Rim Seals," *ASME J. Eng. Gas Turbines Power*, **139**(3), p. 032501.

[15] Horwood, J. T. M., Hualca, F. P., Scobie, J. A., Wilson, M., Sangan, C. M., Lock, G. D., "Experimental and Computational Investigation of Flow Instabilities in Turbine Rim Seals," ASME *J. Eng. Gas Turbines Power*, **141**(1), p. 011028.

[16] Jackson, R., Tang, H., Scobie, J., Owen, J. M., and Lock, G. D., 2021, "Measurement of Heat Transfer and Flow Structures in a Closed Rotating Cavity," ASME Paper No. GT2021-59605. [Submitted]

[17] Luberti, D., Patinios, M., Jackson, R., Tang, H., Pountney, O., Scobie, J., Sangan, C., Owen, J. M., and Lock, G. D., 2020, "Design and Testing of a Rig to Investigate Buoyancy-Induced Heat Transfer in Aero-Engine Compressor Rotors," ASME *J. Eng. Gas Turbines Power*

## APPENDIX: ADDITIONAL FREQUENCY SPECTRUM ANALYSIS

Figure A.1 shows the measured circumferential pressure distribution from the example case in Section 3.1 where $Re_\phi = 8 \times 10^5$, $\beta \Delta T = 0.28$, $Gr = 1.9 \times 10^{11}$ and $Ro = 0.2$. The data is averaged over 50 structure revolutions where the rotational frequency of the structures was stable. A frequency component which is of a higher order than the fundamental ($f_{s,1}$) is required to reconstruct the 'skewed' sinusoid pressure distribution. A curve of the following form is also plotted in Fig. A.1 and provides a close fit to the experimental data:

$$C_p = 0.043 \sin\left(2\pi f_{s,1} t\right) - 0.014 \cos\left(2\pi \left(2 f_{s,1}\right) t\right) \qquad \text{(A.1)}$$
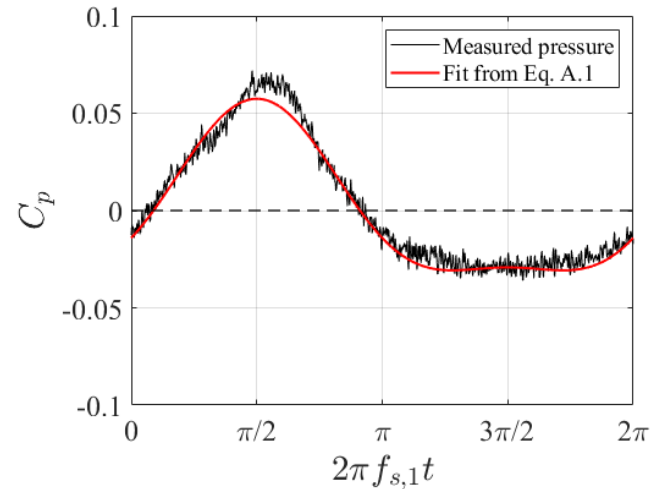


**Figure A.1: Measured circumferential pressure distribution and fitted curve from Eq. A.1.**

The corresponding frequency spectra of the two curves are shown in Fig A.2. The frequency spectrum of the experimental data is found from the same 50 revolutions that construct the above ensemble average. The frequency spectrum of the fitted curve is almost identical, with the magnitude of the peaks matching closely with the measured data. This clearly demonstrates that the second, smaller peak is caused by the asymmetry in the pressure distribution.
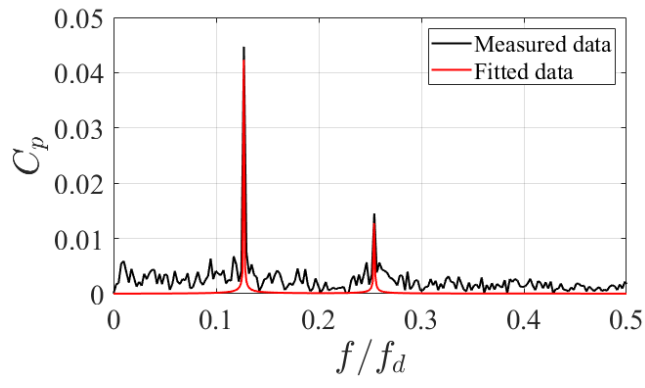


**Figure A.2: Frequency spectra of the measured pressure and fitted pressure distributions.**